

The role of the internal demagnetizing field for the dynamics of a magnonic crystal

M. Langer,^{1,2} F. Röder,^{1,3,4} R. A. Gallardo,⁵ T. Schneider,^{1,6} S. Stienen,¹ C. Gatel,⁴
R. Hübner,¹ L. Bischoff,¹ K. Lenz,¹ J. Lindner,¹ P. Landeros,⁵ and J. Fassbender^{1,2}

¹Helmholtz-Zentrum Dresden – Rossendorf, Institute of Ion Beam Physics and Materials Research,
Bautzner Landstr. 400, 01328 Dresden, Germany

²Institute for Physics of Solids, Technische Universität Dresden, Zellescher Weg 16, 01069 Dresden, Germany

³Triebenberg Laboratory Institute of Structure Physics,
Technische Universität Dresden, 01062 Dresden, Germany

⁴CEMES-CNRS and Université de Toulouse, 29 Rue Jeanne Marvig, F-31055 Toulouse, France

⁵Departamento de Física, Universidad Técnica Federico Santa María,
Avenida España 1680, 2390123 Valparaíso, Chile

⁶Department of Physics, Technische Universität Chemnitz,
Reichenhainer Str. 70, 09126 Chemnitz, Germany

(Dated: December 28, 2021)

Magnonic crystals with locally alternating properties and specific periodicities exhibit interesting effects, such as a multitude of different spin-wave states and large band gaps. This work aims for demonstrating and understanding the key role of local demagnetizing fields in such systems. To achieve this, hybrid structures are investigated consisting of a continuous thin film with a stripe modulation on top favorable due to the adjustability of the magnonic effects with the modulation size. For a direct access to the spin dynamics, a magnonic crystal was reconstructed from ‘bottom-up’, i.e., the structural shape as well as the internal field landscape of the structure were experimentally obtained on the nanoscale using electron holography. Subsequently, both properties were utilized to perform dynamic response calculations. The simulations yield the frequency-field dependence as well as the angular dependence of spin waves in a magnonic crystal and reveal the governing role of the internal field landscape around the backward-volume geometry. The complex angle-dependent spin-wave behavior is described for a 360° in-plane rotation of an external field by connecting the internal field landscape with the individual spin-wave localization.

PACS numbers: 76.50.+g, 75.30.Ds, 75.78.-n, 75.78.Cd, 42.40.-i

I. INTRODUCTION

Magnetic meta-materials, especially magnonic crystals (MCs),^{1–5} experience a growing scientific attention due to many promising applications for future devices in information technology. The root of this development lies in the unique properties of MCs,^{6–8} such the large band gaps and a multitude of adjustable magnon bands.^{7,9–14} Both can be engineered or even tuned by modifying their structural or magnetic properties.^{15,16} In addition, MCs, in particular one-dimensional systems, possess the possibility of reprogramming the magnonic properties by a switching between different states in the magnetic hysteresis.^{17–22} In previous studies, it was already shown that MCs can be used as grating couplers,²³ for magnonic logic,^{24–27} filter²⁸ and sensor²⁹ applications, and moreover, as a tool to access important material properties, such as the exchange constant, at high precision.³⁰

In order to investigate the effect of the internal demagnetizing field H_d^{int} on the spin-wave properties, the dynamics of a surface-modulated magnonic crystal (SMMC)^{31–33} were reconstructed from ‘bottom-up’ as sketched in Fig. 1. This means, the structural shape as well as the projected demagnetizing field were mapped on the nanoscale (see Fig. 1(c)) via high-resolution magnetic imaging using electron holography—a phase retrieval method in transmission electron microscopy (TEM).³⁴

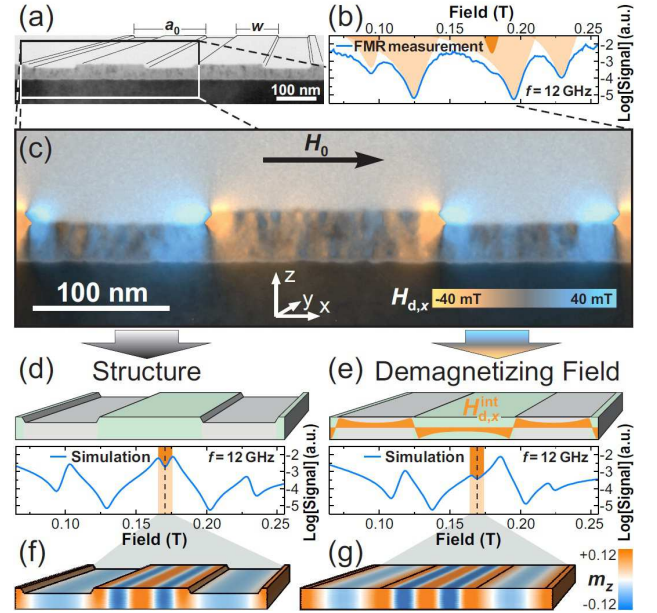


FIG. 1. (Color online) The strategy to understand the spin-wave dynamics of a magnonic crystal. (a) Cross-sectional TEM image with (b) the measured FMR-response (Lorentzian fits in orange). (c) Magnification (black and white) superimposed with the x -component of the simulated demagnetizing field (colorplot). (d,e) Both properties are used as input for dynamic response simulations with (f,g) the resulting mode profiles of the highlighted resonance peaks.

The results were used to reconstruct the dynamic eigenmodes of the system employing micromagnetic simulations (Fig. 1(d,e)). Comparing the results with the measurement (Fig. 1(b)) yields the corresponding spin-wave states (Fig. 1(f,g)) and allows to assess the role of the internal field landscape for the dynamics of the magnonic crystal. Using ferromagnetic resonance measurements and micromagnetic simulations, the in-plane frequency-field dependence and the in-plane angular dependence of the magnonic crystal are studied together with the spin-wave mode profiles.

The important role of the internal demagnetizing field for the dynamics of MCs is demonstrated. Namely, it acts locally as demagnetizing *and* magnetizing field. This study gains a fundamental understanding of the frequency-dependent spin-wave properties in MCs. The spin-wave behavior is examined under the rotation of the external field from the backward-volume ($\mathbf{k} \parallel \mathbf{M}$) to the Damon-Eshbach geometry ($\mathbf{k} \perp \mathbf{M}$) where \mathbf{k} denotes the in-plane wave vector and \mathbf{M} the magnetization. The angular dependence is described using the internal demagnetizing field as well as the mode localization for the estimation of an effective mode anisotropy.

II. THEORY

The spin-wave dispersion³⁵ is the theoretical fundament for the frequency- and angle-dependent resonance equation, which is equivalently formulated in Ref. [33]:

$$\left(\frac{\omega}{\gamma}\right)^2 = H_Y(k) \cdot H_Z(k) \quad (1)$$

with the stiffness fields

$$H_Y(k) = \mu_0 H_0 + \mu_0 M_S [1 - F(kd)] \sin^2 \varphi_k + Dk^2 \quad (2)$$

$$H_Z(k) = \mu_0 H_0 + \mu_0 M_S F(kd) + Dk^2 \quad (3)$$

Here, $f = \omega/(2\pi)$ is the spin-wave frequency, γ the gyromagnetic ratio, H_0 the external magnetic field, M_S the saturation magnetization, $D = 2A/M_S$ the exchange stiffness with A being the exchange constant and φ_k is the angle between magnetization and the wave vector \mathbf{k} . The latter is quantized when tiny periodic thickness variations ($\Delta d \ll d$) are present at the surface. This circumstance leads to the occurrence of standing spin-wave modes with the wave vectors $k = 2\pi n/a_0$ and $n = 1, 2, \dots$ where a_0 is the patterning periodicity. The term $F(kd) = [1 - \exp(-kd)]/(kd)$ in Eqs. (2),(3) is derived from the dipolar interaction with d being the film thickness. Note that the Eqs. (1)–(3) are only valid in the continuous thin film limit and do not account for any coupling of different spin-wave states. Furthermore, a constant magnetization profile with parallel alignment relative to the in-plane oriented external field $\mu_0 H_0$ is assumed. However, it will be shown in Sec. VC that Eqs. (1)–(3) provide a reasonable estimation of the

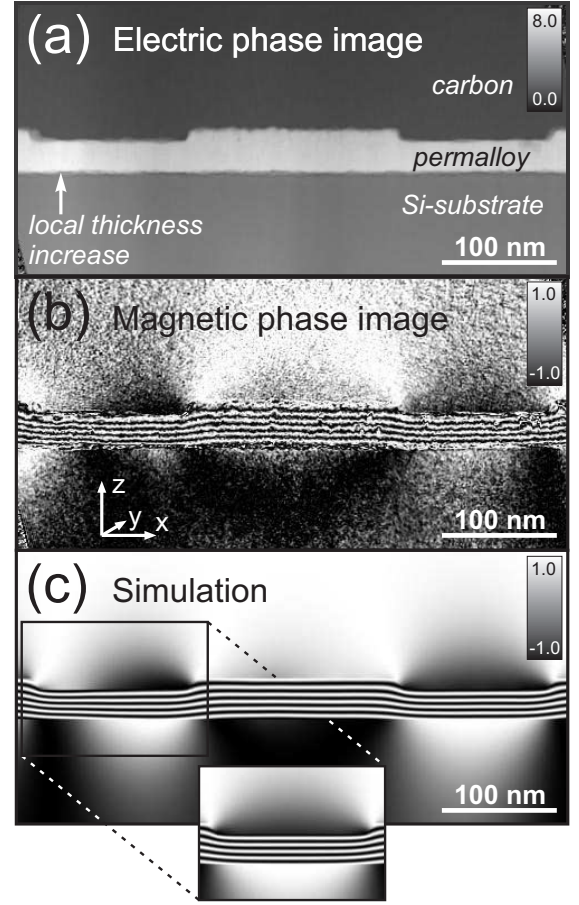


FIG. 2. (a) Electric phase image of the cross-section of a surface-modulated magnonic crystal (SMMC) with 10 nm modulation height. The contrast is proportional to the lamella thickness t in y -direction. (b) Cosine of the 20 times amplified magnetic phase indicating the field lines of the projected x, z components of \mathbf{B} . (c) Simulation of the magnetic phase considering thickness variations (see appendices (ii,iii)). The inset depicts the simulated magnetic phase of the marked area without variations assuming a constant thickness of $t_{\text{avg}} = 38.3$ nm instead.

spin-wave resonance fields if the investigated spin wave branches are (i) far away from crossing points in the $f(H_0)$ dependence (such that effects of mode-coupling can be neglected) and (ii) if the film thickness d and the internal demagnetizing field H_d^{int} at the excited location of the structure are known.

Furthermore, this research employs semi-analytical calculations of the frequency-dependent spin-wave properties based on the plane wave method (PWM)^{7,36,37} with details provided in Ref. [38].

III. MICROMAGNETIC SIMULATIONS

Two kinds of micromagnetic simulations were performed as part of this research, (i) *static* simulations and

(ii) simulations of the *dynamic* FMR response. They were calculated using the *MuMax3*-code³⁹ in two different ways, either by continuous wave⁴⁰ or by pulsed⁴¹ excitation. Further details can be found in the appendices (iv,v).

IV. EXPERIMENTAL DETAILS

A. Sample Fabrication

Initially, a polycrystalline $d = 36.8$ nm thin permalloy ($\text{Ni}_{80}\text{Fe}_{20}$) film was deposited on a surface-oxidized silicon substrate by electron beam physical vapor deposition. To achieve an alternating film thickness, the surface was pre-patterned by means of electron beam lithography. Here, ma-N 2401 negative resist was employed and structured into a stripe mask with $a_0 = 300$ nm periodicity and an individual nominal stripe width of $w = 166$ nm. Subsequently, the uncovered magnetic material was exposed to Ar-ion milling and 10 nm of the magnetic material were removed.³⁰ In this manuscript, the resulting structure is referred to as a surface-modulated magnonic crystal.

B. Electron Holography

Off-axis electron holography⁴² was employed as a unique technique to quantitatively map the projected magnetic induction⁴³ at a spatial resolution of about $2\pi/100$ rad. The imaging of the lamella was carried out in remanence using a HITACHI HF3300 (I2TEM) transmission electron microscope with a 300 kV cold field emission gun and two goniometer stages (a field-free Lorentz stage and a standard high resolution stage).

Dedicated Lorentz modes combined with the CEOS B-cor corrector allow to achieve a 0.5 nm spatial resolution in a field-free environment (less than 0.1 mT). All holograms were recorded in double-biprism configuration⁴⁴ to avoid Fresnel fringes and to independently set the interface area and the fringe spacing. At a tilt of 30° of the lamella's long direction (x) with respect to the optical axis (y), the sample was initially saturated by means of the objective lens field. More details regarding the measurement technique are provided in the appendix (ii). Furthermore, information regarding the setup can be found in Ref. [45].

The resulting electric and magnetic phase images are illustrated in Fig. 2(a-b). The electric phase is sensitive to different materials as well as the thickness along the beam axis. The magnetic phase (here: the 20 times amplified cosine) depicted in Fig. 2(b) appears as black and white lines reflecting the local orientation of the projected in-plane \mathbf{B} field with the absolute gradient being proportional to its magnitude.

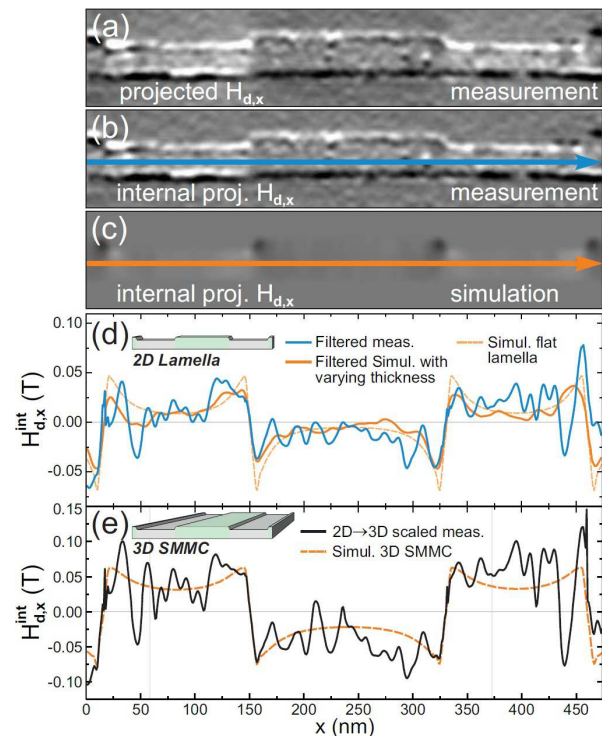


FIG. 3. (Color online) (a) Experimentally projected x -component of the demagnetizing field $H_{d,x}$ smoothed using a Gaussian filter. (b) Same as (a) but with external $H_{d,x}$ field projection subtracted. (c) Simulation of the internal $H_{d,x}$ field. (d) The vertically averaged internal $H_{d,x}$ field obtained by measurement [blue arrow in (b)] and simulation [orange arrow in (c)] normalized by the thickness profile. (e) Due to the small thickness of the lamella, the internal $H_{d,x}$ field is scaled in order to resemble a 3D structure with continuous magnetic material along the y -axis (see appendix (iii) for details).

As explained in the appendices (ii,iii), the local thickness distribution in beam direction (plotted in Fig. 10–appendix) could be obtained from the electric phase. Together with the 2D structural information according to Fig. 2(a), both were employed to reconstruct the remanent state of the lamella via static micromagnetic simulations.³⁹ The resulting simulated magnetic phase is shown in Fig. 2(c). Useful for comparison is an additional simulation where the thickness variations were not considered, as shown in the inset of Fig 2(c).

The simulation exhibits very similar features compared to those obtained by the measurement. The phase irregularities mapped on the left side of the structure were reproduced by the simulation in Fig. 2(c) and can be related to a local thickness increase, since the features vanish (see inset in 2(c)) when a flat lamella is assumed.

Next, the vertically averaged distribution of the internal demagnetizing field $H_{d,x}^{int}(x)$ along the lamella's long axis was extracted. To achieve this, the major contribution of the magnetization was gained and subtracted from the measured projected magnetic phase by reemploying the above mentioned static simulations. Figure 3(a) illus-

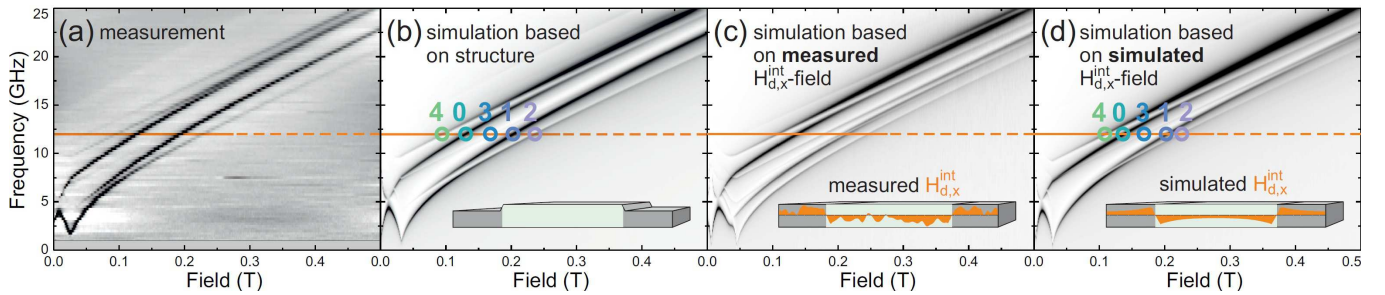


FIG. 4. (Color online) $f(H_0)$ dependences of the surface-modulated magnonic crystal with the gray scale representing the dynamic response. (a) Measurement and (b-d) different simulations of the FMR response. (b) Simulation based on the structural shape of the magnonic crystal. In (c-d) the internal demagnetizing field $H_{d,x}^{\text{int}}$ was added to a 36 nm thin film with subsequent calculation of the FMR response. (c) is based on the measured $H_{d,x}^{\text{int}}$ field and (d) on the simulated one.

trates the resulting 2D distribution of the magnetic phase generated by the $H_{d,x}$ field with white (black) color representing a positive (negative) sign of $H_{d,x}$. This means that $H_{d,x}$ is acting as *demagnetizing* or *magnetizing* field, respectively. Figure 3(b) only depicts the projected internal $H_{d,x}$ field isolated by subtraction of the contrast generated by the simulated stray field *outside* the magnetic structure. Hence, the stray field features above the SMMC in Fig. 3(a) vanish in 3(b). Moreover, there are parasitic contribution to the projected internal field due to the external strayfield in the front and in the back of the lamella with respect to the beam direction. Such contributions were also estimated using the static micromagnetic simulations.

In Fig. 3(d) the vertically averaged profiles of $H_{d,x}^{\text{int}}$ are presented according to the arrows in Figs. 3(b-c). The values taken from Figs. 3(b-c) are normalized by the lamella thickness profile discussed in the appendix (iii). Blue color represents the measurement and orange color the simulation. The profiles demonstrate a very good agreement between both the measurement and the simulation and are corroborated with the simulated $H_{d,x}^{\text{int}}(x)$ -distribution of a flat structure (orange dashed line), where the lamella thickness was fixed to t_{avg} .

Since further investigations focus on a 3D extended MC and not on a thin (2D) lamella structure, systematic difference between the internal fields of both systems need to be considered. As further described in the appendix (iii), this circumstance is addressed by a scaling of $H_{d,x}^{\text{int}}(x)$ with the result shown as black solid line in Fig. 3(e). Apart from the apparent oscillations arising from measurement noise, the result matches well the distribution obtained by the simulation (orange dashed line in Fig. 3(e)) of an ideal 3D SMMC.

C. Magnetic Characterization

The magnetic characterization was carried out using a broadband vector network analyzer ferromagnetic resonance (FMR) setup as described in Refs. [30,46]. Excitation of the spin system is achieved by coupling a microwave signal via a coplanar waveguide to the surface of a ‘flip-chip’-mounted sample. The transmission signal S_{21} is measured at several fixed excitation frequencies f sweeping the external field H_0 . The absolute value of S_{21} was recorded as the FMR-response.

tation of the spin system is achieved by coupling a microwave signal via a coplanar waveguide to the surface of a ‘flip-chip’-mounted sample. The transmission signal S_{21} is measured at several fixed excitation frequencies f sweeping the external field H_0 . The absolute value of S_{21} was recorded as the FMR-response.

V. RESULTS AND DISCUSSION

In this section, the results from two independent approaches to reconstruct the effective spin-dynamics in a magnonic crystal are discussed. With both the knowledge of (i) the structural shape and (ii) the internal $H_{d,x}$ field, dynamic simulations were performed.

A. Frequency dependence in backward-volume geometry

Figure. 4 illustrates several $f(H_0)$ dependences obtained from measurement and simulations. In 4(a) the measured $f(H_0)$ is shown whereas 4(b) was obtained from the remodeling of the sample structure and subsequent FMR simulations. The evident similarity between both indicates a reliable representation of the sample structure by the micromagnetic model. In contrast, Fig. 4(c) and (d) are obtained by simulating a 36 nm thin permalloy film with a virtually added periodic distribution of $H_{d,x}^{\text{int}}$. In 4(c) the *measured* field distribution was employed and in 4(d) the *simulated* one was taken corresponding both to the two plots in Fig. 3(e). A convincing qualitative agreement of all shown $f(H_0)$ dependences with the measurement is obtained.

However, at second glance, a higher number of modes can be found in Fig. 4(c), which is due to the measurement noise in $H_{d,x}^{\text{int}}$ violating the mirror symmetry of the internal field landscape. Especially at the edges of the thick part, the different local demagnetizing fields lead to the occurrence of two separate *non-symmetric* edge modes with different energies. However, for the symmetric $H_{d,x}^{\text{int}}$ field in Fig. 3(d), the $f(H_0)$ matches well the one

obtained in Fig. 3(b) with similar mode characteristics.

B. Mode profiles

Another way to test the level of similarity between the different simulations presented above is to analyze the mode profiles. In Fig. 5 the profiles of the resonant spin waves at $f = 12$ GHz are plotted and labeled with the respective mode number n . The plots indicate a convincing agreement between both simulations such that the individual character of the plotted mode profiles reflects similar physics. Consequently, the dynamics of the SMMC is very similar to flat MC with a pronounced internal field structure, such as bi-component MCs. The dynamics of such systems can be well described by the plane wave method,^{7,36–38} which was used in addition for the calculation of the mode profiles in Fig. 5 confirming the results from the simulations. Note that the frequency of 12 GHz was selected such that effects from mode coupling are small and, thus, can be neglected in the following discussion.

The reason for the multitude of measurable spin-wave modes in SMMCs is explained by Fig. 6(a). Here, the $f(H_0)$ dependence of the modes in the limit of a thin film with tiny modulation $\Delta d \rightarrow 0$ is plotted. Apart from the uniform mode, standing spin-wave modes are present, with a defined number of nodes ($2n$) fitting in one period a_0 as sketched in the inset of Fig. 6(a). This circumstance results in a quantization of the wave vector with $k = 2\pi n/a_0$. By applying Eqs. (1)–(3), the corresponding frequency dependence can be obtained (orange lines). The standing spin-wave modes can couple to the uniform mode and together form the full spectrum of possible states accessible in such structures.^{30,32,33} In Fig. 6(a), at the marked frequency of 12 GHz, three states with lower energy than the uniform one with $n = 1, 2, 3$ are found and with the $n = 2$ state being lowest. Note that for a given frequency, the mode energy is reflected by the resonance field such that for low (high) energy modes a high (low) external field must be supplied to resonate at the same frequency. Thus, at $f = \text{const.}$, high resonance fields represent low mode energy and reverse.

For an SMMC with a pronounced modulation, these states are present as well, but are shaped differently by the internal field landscape. In Fig. 5, all modes can still be identified according to their total number of nodes ($2n$) inside a period a_0 . However, due to the presence of the internal field landscape, the modes can no longer be described assuming a constant wave vector due to $k = 2\pi n/a_0$ and an extension over the full MC. Instead, the modes 0–3 reveal a clear localization in either the thick or the thin part and all modes show major deviations from the harmonic character sketched in the inset of Fig. 6(a), which can only be explained with the help of the internal field landscape shown in Fig. 6(b). The field distribution (orange) is translated into a region map (roman numbers) of negative (I,II) and positive (III,IV)

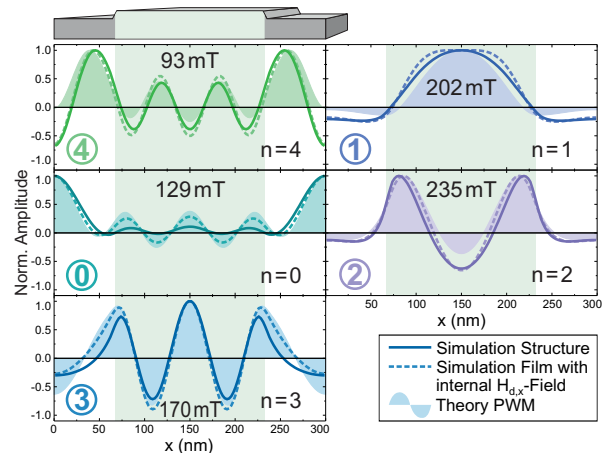


FIG. 5. (Color online) Mode profiles of spin-waves (with corresponding mode number n) at different resonance positions as marked in Figs. 4 and 8. They are derived by simulations and PWM theory.

internal fields. The dashed lines represent the part of the field landscape where the respective mode energy is sufficient for a spin-wave excitation.

In order to understand the characteristic mode profiles in Fig. 5, it is useful to know the dependence of the wave vector k on the effective field $H_{\text{eff}}^n = H_0^n + H_{\text{d}}^{\text{int},n}$. At this point, the knowledge of the internal demagnetizing field $H_{\text{d}}^{\text{int}}$ becomes relevant again. As the $H_{\text{d}}^{\text{int}}$ field itself depends on the location along the x -axis, the distribution $H_{\text{d}}^{\text{int}}(x)$ can be used to assign a specific k -value with a location inside the MC. Moreover, this relation can be used to identify regions where no k -value can be attributed to the effective field which is important for understanding the individual mode localization. For this purpose, the spin-wave dispersion expressed by Eqs. (1)–(3) is employed with H_0 being replaced by the effective field $H_{\text{eff}}^n = H_0^n + H_{\text{d}}^{\text{int},n}$ to consider both, the external field of the n th spin wave in resonance H_0^n as well as the internal demagnetizing field $H_{\text{d}}^{\text{int},n}$. Accordingly, the dependence of the effective field H_{eff}^n on the wave vector k reads (for $\varphi_k = 0^\circ$):

$$\mu_0 H_{\text{eff}}^n = -\frac{1}{2}\mu_0 M_{\text{S}} F + \left[\frac{1}{4}(\mu_0 M_{\text{S}} F)^2 + \left(\frac{\omega}{\gamma} \right)^2 \right]^{\frac{1}{2}} \quad (4)$$

Eq. (4) can now be used, to correlate the wave vector with the effective field at $f = 12$ GHz, which is illustrated in Fig. 7(a) for both the thick and the thin part of the MC. With the given resonance fields in Fig. 5 and the knowledge of the internal demagnetizing field $H_{\text{d}}^{\text{int}}(x)$, the effective fields can be calculated for all different locations in the SMMC and for each spin-wave mode. The colored lines in Fig. 7(a) correspond to the range of k -values associated with the internal field landscape for each mode. Bright colors represent the edge regions (I,IV) and dark colors represent the center regions (II,III). In Fig. 7(b), the $H_{\text{d}}^{\text{int}}(x)$ distribution (orange dashed line in Fig. 3(e))

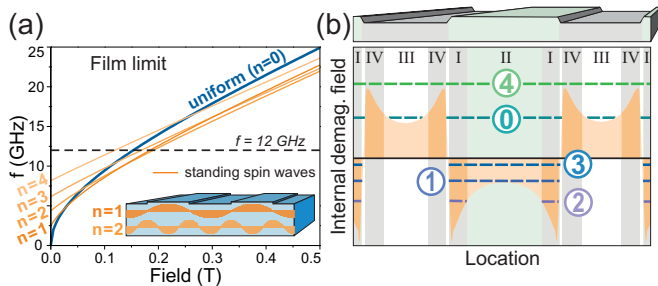


FIG. 6. (Color online) (a) $f(H_0)$ in the film limit with tiny modulation. Standing spin-waves modes appear quantized due to $k = 2\pi n/a_0$ and are sketched in the inset. (b) Mode localization and internal field landscape of an SMMC. The H_d^{int} field is negative in region I and II and positive in region III and IV. Thus, modes with energy below the uniform mode (flat black line) can only be excited in the regions where the internal field is reduced (I,II).

is used, to calculate the wave vector dependent on the location along the x -axis.

With Fig. 7(a) and (b), the reason for the mode localization can be explained. For modes 1–3, the effective field in the thin part (III,IV) exceeds 176 mT, which is maximum value (vertex of the gray parabola in 7(a)) for a defined spin-wave excitation in this region. Thus, all three modes localize in the thick part (I,II) and avoid the regions III and IV. Moreover, the calculations reveal that mode 2 is only excited at the edges of the thick part (I).

It is important to note that in SMMCs with a pronounced modulation, a classical uniform mode cannot exist due to the variance of the internal fields. Instead, mode 0 behaves as a quasi-uniform excitation of the center of the thin part (III,IV) of the MC, which is supported by the mode profile in Fig. 5 and by the range of k -values in Fig. 7(b) reaching almost perfectly $k = 0$ in the center of part III. Unlike the higher modes 2–4, the wave vector of mode 0 and mode 1 is not only delimited by the vertices of the parabola in Fig. 7(a) where the energy becomes too small for a spin-wave excitation. It is also delimited by the uniform state ($k = 0$) at $\mu_0 H_{\text{eff}} = 154$ mT such that regions of lower internal fields cannot be excited anymore. Due to that reason, mode 0 avoids the thick part (I,II) as much as mode 1 avoids region I as shown in Fig. 7(b) and confirmed by Fig. 5.

The only mode with sufficient energy to spread over the full MC is mode 4. In Fig. 7(a) and (b) the distribution of the modes' wave vector is plotted according to Eq. (4). Expressed vividly, the mode can rearrange its 8 nodes in a way that the energy of the mode is distributed equally over the full structure. The number of nodes in the thick part m and in the thin part l can be estimated by solving $\mu_0 H_0^{\text{thick}} = \mu_0 H_0^{\text{thin}}$, i.e. $\mu_0 H_0^m (d = 36 \text{ nm}, \mu_0 H_d^{\text{thick}} = -39 \text{ mT}, k = \frac{m\pi}{w}) = \mu_0 H_0^l (d = 26 \text{ nm}, \mu_0 H_d^{\text{thin}} = 41 \text{ mT}, k = \frac{l\pi}{a_0 - w})$

with $n = m + l$ and with H_d^{thick} and H_d^{thin} being the average internal demagnetizing fields of the thick and the

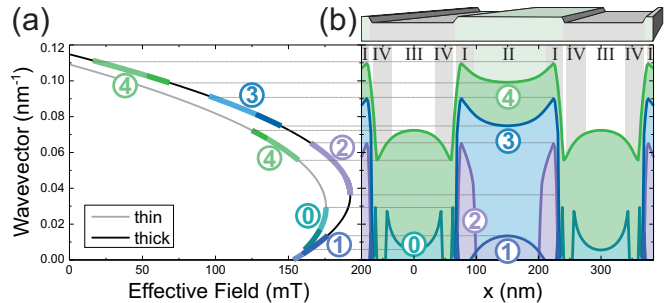


FIG. 7. (Color online) wave vector calculation for the resonances marked in Fig. 5 dependent on (a) the effective field and (b) the location along the x -axis. For modes 1–3, the internal fields in the thin part are so high that the effective field exceeds the vertex of the parabola in (a) and thus, this region is avoided. In (a) bright lines correspond to the edge (I,IV) and dark lines correspond to the center regions (II,III).

thin part of the MC. Applying Eq. (4) yields a resonance field of $\mu_0 H_0^m = \mu_0 H_0^l = 103$ mT and the node numbers $m = 5.29$ and $l = 2.71$, which is coherent with the node distribution in Fig. 5.

In short, it is observed, that three kinds of modes are distinguished in the SMMC. (i) A quasi-uniform central excitation of the thin part of the SMMC, which corresponds to mode 0. (ii) $k \neq 0$ modes with sufficient energy to extend over the full MC (e.g. mode 4) and (iii) $k \neq 0$ modes with insufficient energy enforcing a localization in the thick part (I,II) of the MC, such as mode 1–3.

Modes of category (ii) adapt their wave vector such that the mode energy is equally distributed over the full structure while the total number of nodes ($2n = m + l$) is conserved. For these modes, the wave vector must be calculated separately for both the thick and the thin part as explained above. This is different for the category (iii) of localized modes. These modes exhibit a ‘damped’ trough in the thin part where the local fields are too high for a spin-wave excitation. The residual $2n - 1$ nodes of the modes are condensed in the thick part, where the internal field is reduced. Accordingly, the wave vector of these modes is shifted to $k = (2n - 1)\pi/w$ instead of $2\pi n/a_0$ in the thin film limit.

C. Angular Dependence

Figure 8(a) shows the measurement and 8(b) the simulation of the angular dependence at $f = 12$ GHz. The backward-volume direction ($\varphi_H = 0^\circ, 180^\circ$) is marked by the orange line with the labeled resonances being the same as in Fig. 4(b). $\varphi_H = 90^\circ$ and 270° both correspond to the Damon-Eshbach geometry. Again, a satisfactory reconstruction of the measurement by the simulation based on the sample structure is obtained.

The most prominent resonance branch is the flat one between 45° – 135° and 225° – 315° . This mode corresponds to the uniform mode around the Damon-Eshbach

geometry with negligible internal demagnetizing fields. In the same angular range, there is a second less noticeable resonance branch observed at lower external fields corresponding to the $n = 1$ Damon-Eshbach mode. Knowing that the $n = 1$ mode is identified at $\mu_0 H_0 = 202$ mT in the backward-volume direction, mode 1 can be followed through a full 360° rotation of the external field.

In order to analytically express the angular dependence of a mode, Eqs. (1)–(3) can again be employed together with the identity $\varphi_k = \varphi_H$. Around the backward-volume direction, the high internal demagnetizing fields must also be taken into account with regard to the individual mode localization. In order to include the demagnetizing field into the angle-dependent spin-wave dispersion, $\mu_0 H_0$ was replaced by $\mu_0 H_0 + \mu_0 H_d \cdot \cos(2\varphi_H)$ in Eq. (2) and by $\mu_0 H_0 + \mu_0 H_d \cdot \cos^2\varphi_H$ in Eq. (3) analogous to the description of a uniaxial anisotropy field.^{46–48} From Eqs. (1)–(3), a modified angular dependence is obtained

$$\begin{aligned} \mu_0 H_0^n(\varphi_H) = & -\frac{1}{2}\mu_0 H_d (\cos(2\varphi_H) + \cos^2\varphi_H) - Dk^2 \\ & -\frac{1}{2}\mu_0 M_S F - \frac{1}{2}\mu_0 M_S (1-F) \sin^2\varphi_H + \left[\frac{1}{4}\mu_0^2 H_d^2 \sin^4\varphi_H \right. \\ & + \frac{1}{2}\mu_0^2 H_d M_S F \sin^2\varphi_H - \frac{1}{2}\mu_0^2 H_d M_S (1-F) \sin^4\varphi_H \\ & \left. + \frac{1}{4}(\mu_0 M_S F - \mu_0 M_S (1-F) \sin^2\varphi_H)^2 + \left(\frac{\omega}{\gamma}\right)^2 \right]^{\frac{1}{2}} \end{aligned} \quad (5)$$

with $\mu_0 H_0^n$ the resonance field of the n th mode. The angle-dependent resonance fields are calculated using Eq. (5) employing simplified assumptions: (i) The wave vector of localized $k \neq 0$ modes is defined by $k = (2n - 1)\pi/w$ and (ii) for the effective demagnetizing field H_d^{eff} the average value of the regions in which the modes localizes is taken. (iii) As explained in Sec. VB, for modes localized in the thick as well as the thin part of the MC (e.g. mode 4), the node number and the effective field H_d^{eff} are calculated separately for both parts.

The calculated angle dependences according to Eq. (5) are depicted in Fig. 8 as solid lines revealing a firm overall agreement to the measurement and the simulation. The parameters used for the calculations according to the above assumptions are provided in table I. Mode 3 is the only one with major deviations from the resonance positions in the colorplot. The discrepancy is likely due a different pinning condition at the edge of the thick part resulting in an overestimation of the wave vector by $k = (2n - 1)\pi/w$. This is supported by the mode profile in Fig. 5 revealing a reduced wave vector between the film limit $2\pi n/a_0$ and $(2n - 1)\pi/w$. A fitting angle-dependent resonance position can be obtained for $k = 4.3\pi/w$ (blue dot-dashed line in Fig. 8(b)), which is coherent with the number of nodes in Fig. 5.

For the calculations in and around the Damon-Eshbach geometry, the internal demagnetizing fields were neglected, i.e. , $\mu_0 H_d^{\text{eff}} = 0$. Interestingly, a reliable reproduction of the behavior of mode 1 (dark blue line in

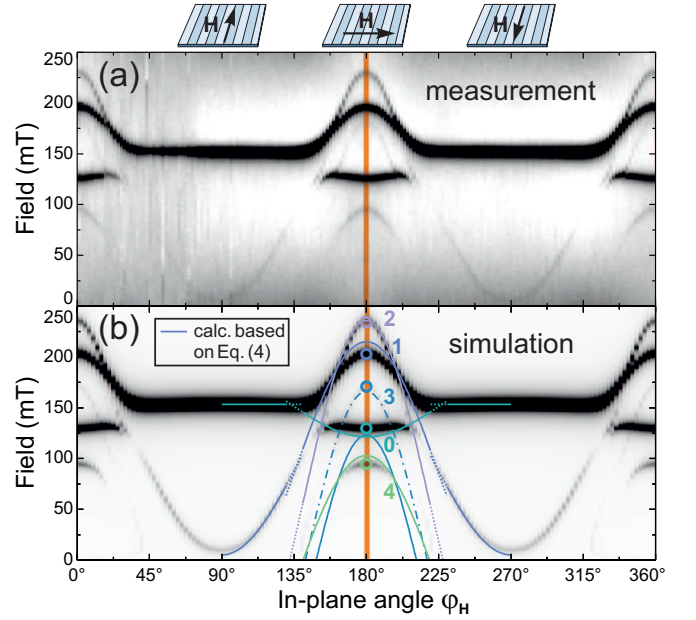


FIG. 8. (Color online) In-plane angular dependence of the resonance fields of an SMMC with 10 nm modulation height, where (a) is the measurement and (b) the corresponding simulation. The numbered resonances correspond to the mode profiles shown in Figs. 5. The solid lines are calculations based on Eq. (5) with parameters accounting for $\varphi_H = 135^\circ - 225^\circ$ provided in table I. For $\varphi_H = 225^\circ - 270^\circ$, mode 1 was described without consideration of an internal demagnetizing field assuming a film thickness of $d = 26$ nm.

Fig. 8(b)) can only be obtained if a dynamically active film thickness of only $d = 26$ nm (corresponding to the thin part) is assumed.

VI. CONCLUSION

Electron holography measurements were employed to map the internal magnetic field landscape of a surface modulated magnonic crystal on the nanoscale. The measurements confirmed the alternating character of the demagnetizing field acting locally as demagnetizing- and

TABLE I. Parameters used for the calculation angular dependence of the spin waves between $\varphi_H = 135^\circ - 225^\circ$.

mode no.	n	localisation	d (nm)	k_{eff}	$\mu_0 H_d^{\text{eff}}$ (mT)
0		III	26	0	31.9
1		II	36	π/w	-31.8
2		I	36	$3\pi/w$	-57.0
3		I,II	36	$5\pi/w$	-38.7
4		I-IV	26	$\frac{2.71\pi}{a_0-w}$	-38.7
			36	$5.29\pi/w$	40.9

magnetizing field. Micromagnetic reconstructions of its dynamic behavior revealed the dominating role of the magnonic crystals' internal demagnetizing field. The significant impact of the internal field landscape on the mode profiles and the modes' angular dependences were discussed.

VII. ACKNOWLEDGMENT

We thank B. Scheumann for the film deposition, A. Kunz for the FIB lamella preparation and Y. Yuan and S. Zhou for the VSM characterization as well as H. Lichte for fruitful discussions. Support by the Nanofabrication Facilities Rossendorf at IBC as well as the infrastructure provided by the HZDR Department of Information Services and Computing are gratefully acknowledged. Our research has received funding from the Graduate Academy of the TU Dresden, from the European Union Seventh Framework Program under grant no. 312483-ESTEEM2 (Integrated Infrastructure Initiative-I3), the Centers of Excellence with Basal/CONICYT financing (grant no. FB0807), CONICYT PAI/ACADEMIA 79140033, FONDECYT 1161403, CONICYT PCCI (grant no. 140051) and DAAD PPP ALECHILE (grant no. 57136331) and from the Deutsche Forschungsgemeinschaft (grant no. LE2443/5-1).

VIII. APPENDIX

This section contains details regarding (i) the fabrication of the TEM lamella, (ii) the electron holography technique, (iii) the extraction of the internal demagnetizing field and (iv) the static and (v) the dynamic simulations carried out in this work.

(i) Lamella Fabrication The cross-sectional TEM lamella of the magnonic crystal was prepared by in-situ lift-out using a Zeiss Crossbeam NVision 40 system. In order to protect the structure surface, a carbon cap layer was deposited by electron beam assisted precursor decomposition and subsequent Ga focused ion beam (FIB) assisted precursor decomposition. Subsequently, the TEM lamella was prepared using a 30 keV Ga FIB with adapted currents. Its transfer to a 3-post copper lift-out grid (Omniprobe) was done with a Kleindiek micromanipulator. To minimize sidewall damage, Ga ions with 5 keV energy were used for final thinning of the TEM lamella until electron transparency was achieved.

(ii) Off-Axis Electron Holography Figure 9(a) illustrates the working principle of an off-axis electron holography setup. Employing a Möllenstedt biprism, the object- and the reference beam is precisely superimposed at the image plane. The recorded interference fringe pattern is shown in Fig. 9(b) with tiny contrast variations and fringe bending (see inset in Fig. 9(b)). The holo-

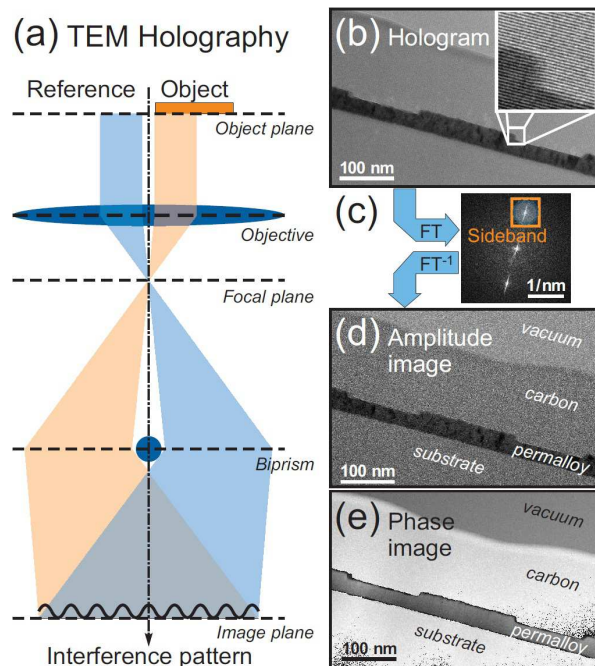


FIG. 9. (Color online) Acquisition and reconstruction scheme of an electron hologram. (a) Setup of electron holography in TEM. (b) Hologram of a permalloy ($\text{Ni}_{80}\text{Fe}_{20}$) thin film with $\Delta d = 10$ nm surface modulation. (c) Fourier spectrum of the hologram showing two sidebands and one center band. The Fourier transform of the upper sideband, low-pass filtered by a numerical aperture, yields the image wave represented by (d) the (wrapped) amplitude and (e) the phase image.

gram is reconstructed by employing the upper sideband of the hologram's Fourier spectrum (see Fig. 9(c)). By inverse Fourier transformation the amplitude and phase information depicted in Fig. 9(d) and Fig. 9(e) are obtained. The phase unwrapping is carried out using the Goldstein algorithm.⁴⁹ The hologram series acquisition (40 holograms for each orientation) and the wave averaging were employed to reduce the phase noise.⁵⁰ Note that displacement removal and first-order aberration corrections were required to match the mean phase.

The electron phase is sensitively altered by electric and magnetic properties of the sample and is, thus, key quantity for the field mapping on the nanoscale³⁴ given by

$$\varphi(x, z) = C_E \int_{t_l(x, z)}^{t_u(x, z)} V(x, y, z) dy - \frac{e}{\hbar} \iint_{\mathbf{S}} \mathbf{B} d\mathbf{A}. \quad (6)$$

The first integral is the projection of the electrostatic potential V along the beam (y -)direction constricted by the local lamella thickness $t(x, z) = t_u - t_l$. The interaction constant C_E is about 0.0065 $(\text{Vnm})^{-1}$ at 300 kV. Being proportional to the magnetic flux of a magnetic induction $\mathbf{B} = \mu_0 \mathbf{H}_d + \mu_0 \mathbf{M}$ through the surface \mathbf{S} enclosed by the object- and the reference beam, the second integral quantifies the magnetic contribution to the phase.

Flipping the sample upside down⁵¹ for a second measurement yields φ_{flipped} , which can be used to separate the electric φ_{el} and magnetic phase shift φ_{mag} as shown in Fig. 2(a-b):

$$\varphi_{\text{el}} = \frac{1}{2}(\varphi + \varphi_{\text{flipped}}) \quad (7)$$

$$\varphi_{\text{mag}} = \frac{1}{2}(\varphi - \varphi_{\text{flipped}}) \quad (8)$$

As evident from Eq. (6), the electric phase contains the full information about the 3D sample geometry, which was further used to rebuild the structure for micromagnetic simulations. As another implication, the gradient of the magnetic phase returns purely the projected in-plane components of the magnetic induction:

$$\begin{aligned} \nabla\varphi_{\text{mag}}(x, z) &= \frac{e}{\hbar} \int_{-\infty}^{+\infty} \mathbf{B} \times d\mathbf{y} \\ &= \mu_0 \frac{e}{\hbar} \left(\int_{t_l(x,z)}^{t_u(x,z)} (\mathbf{M} + \mathbf{H}_d^{\text{int}}) \times d\mathbf{y} + \int_{t_u(x,z)}^{\infty} \mathbf{H}_d^{\text{ext}} \times d\mathbf{y} + \int_{-\infty}^{t_l(x,z)} \mathbf{H}_d^{\text{ext}} \times d\mathbf{y} \right) \end{aligned} \quad (9)$$

To obtain the internal demagnetizing field $\mathbf{H}_d^{\text{int}}$, a decomposition of \mathbf{B} into the magnetization \mathbf{M} and the demagnetizing field \mathbf{H}_d is necessary. A deeper technical description of the acquisition of a TEM hologram is provided in Refs. [42 and 50].

(iii) Internal Demagnetizing Field Extraction

After removing the phase contributions of the external strayfield (see Sec. IV B), the vertically averaged distribution of the internal $H_{d,x}$ field was obtained by employing a numerical mask inside the magnetic region. In order to reduce the number of artifacts, areas of large phase noise were neglected. To achieve absolute field values in Tesla, the integrated magnetic phase was divided by the local lamella thickness (shown in Fig. 10). Here, the field was averaged with the length of the vertical integration path and a Gaussian filter was applied in order to improve the signal-to-noise ratio of the extracted field distribution in Fig. 3(d).

To reconstruct the $H_{d,x}^{\text{int}}(x)$ -distribution of an extended SMMC, a field scaling was necessary (see Sec. IV B) due to two reasons. First, systematic deviations between the thickness-varied and Gaussian filtered simulation (solid orange line in Fig. 3(d)) and the simulation of a perfectly flat lamella (dashed orange line in Fig. 3(d)) were quantified and corrected. Second, the systematic differences of the internal field in a flat ($t_{\text{avg}} = 38.3$ nm thick) 2D structure compared to the field in a 3D magnonic crystal needed to be regarded. Therefore, a scaling function was defined based on the static simulation of a flat quasi 2D lamella (dashed orange line in Fig. 3(d)) and a 3D SMMC (dashed orange line in Fig. 3(e)). Since the field values differ by more than one order of magnitude, the

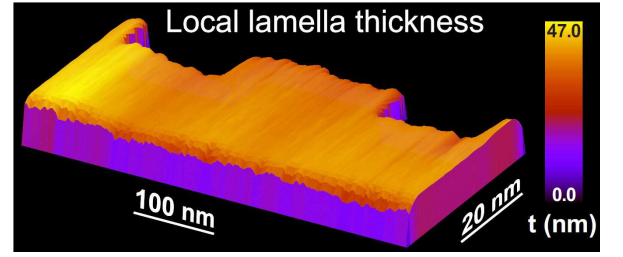


FIG. 10. (Color online) Local lamella thickness t in beam direction determined from the electric phase depicted in Fig. 2(a).

scaling was performed logarithmically:

$$H_{d,x}^{\text{3D}}(x) = \frac{H_{d,x}^{\text{2D}}(x)}{|H_{d,x}^{\text{2D}}(x)|} \cdot |H_{d,x}^{\text{2D}}(x)| \left(\frac{\log |H_{d,x}^{\text{3D,sim}}(x)|}{\log |H_{d,x}^{\text{2D,sim}}(x)|} \right) \quad (10)$$

Here, $H_{d,x}^{\text{3D}}(x)$ denotes the resulting 3D-corrected field measurement and $H_{d,x}^{\text{2D}}(x)$ is the measured distribution of the thin (2D) lamella. The same field distributions obtained by simulations are labeled $H_{d,x}^{\text{3D,sim}}(x)$ and $H_{d,x}^{\text{2D,sim}}(x)$, respectively. Note that the index ‘int’ was omitted in Eq. (10).

(iv) Static Simulations For a thorough reconstruction of the lamella structure, static simulations were carried out. First, the average thickness t_{avg} of a flat lamella was varied until the magnetic phase inside the MC matched the mean phase obtained by measurement. With the help of that, the variations of the electric phase (Fig. 2(a)) inside the MC could be translated into local thickness variations with the result shown in Fig. 10. In order to consider tiny thickness variations in the static simulations, the saturation magnetization was scaled locally by $M_S'(x, y) = t(x, y)/t_{\text{avg}} \cdot M_S$ with a cell size of $2.438 \text{ nm} \cdot 2.125 \text{ nm} \cdot 2.410 \text{ nm}$ for a high resolution. Note that the thickness along the beam axis was fixed to the average value of $t_{\text{avg}} = 38.3$ nm. $M_S = 735$ kA/m, $D = 23.6$ Tnm² and the g -factor $g = 2.11$ were selected according to the material parameters of a permalloy reference film.³⁰

In order to compare a perfect (flat) 2D lamella with a 3D SMMC, the micromagnetic model above was modified omitting the local scaling of M_S with and without periodic boundary conditions in y -direction.

(v) Dynamic Response Simulations The dynamic response simulations³⁹ were performed in two different ways. In order to obtain frequency-field dependencies (see Fig. 4), pulsed⁴¹ simulations were calculated. To simulate the angle-dependent spin-wave resonance (shown in Fig. 8), a continuous-wave approach⁴⁰ was chosen. As the latter does not require Fourier-transformations in frequency-space, such simulations could directly be carried out at $f = 12$ GHz.

Two different simulation geometries were selected: (i) a structural reconstruction of the shape of the magnonic crystal and (ii) an approach using the internal demagnetizing field $H_{d,x}^{\text{int}}(x)$ only as an additive field in a 36 nm thin permalloy film.

For the structural reconstruction of the magnonic crystal, the micromagnetic model according to the electrical phase image of the magnonic crystal (Fig. 2(a)) was applied. Minor changes of the simulation layout according to different *average* values of $a_0 = 300$ nm and $w = 166$ nm were regarded and, furthermore, the geometry was symmetrized. The modulation height was fixed to the value of $\Delta d = 10$ nm with a continuous film

of 26 nm thickness underneath. For an appropriate cross-sectional resolution, a cell size of $2.344 \text{ nm} \cdot 4 \text{ nm} \cdot 2 \text{ nm}$ was chosen with $128 \cdot 16 \cdot 18$ cells in total. In order to realize a continuous elongation of the structure, the geometry was repeated 30 times in the x - and 100 times in the y -direction.

In the second approach, the internal demagnetizing field $H_{d,x}^{\text{int}}(x)$ of the MC was added to an unmodulated continuous thin film. Due to the symmetry in z -direction, a larger cell-size of 12 nm was chosen with 3 cells in total along the z -axis. The cell size and the cell number along the x - and y -axis as well as the 2D repetitions were selected equivalently.

-
- ¹ V. V. Kruglyak, S. O. Demokritov, and D. Grundler, J. Phys. D: Appl. Phys. **43**, 264001 (2010).
- ² G. Gubbiotti, S. Tacchi, M. Madami, G. Carlotti, A. O. Adeyeye, and M. Kostylev, J. Phys. D: Appl. Phys. **43**, 264003 (2010).
- ³ B. Lenk, H. Ulrichs, F. Garbs, and M. Münzenberg, Phys. Rep. **507**, 107 (2011).
- ⁴ M. Krawczyk and D. Grundler, J. Phys. Condens. Matter **26**, 123202 (2014).
- ⁵ A. V. Chumak, V. I. Vasyuchka, A. A. Serga, and B. Hillebrands, Nat. Phys. **11**, 453 (2015).
- ⁶ S. Tacchi, G. Duerr, J. W. Klos, M. Madami, S. Neusser, G. Gubbiotti, G. Carlotti, M. Krawczyk, and D. Grundler, Phys. Rev. Lett. **109**, 137202 (2012).
- ⁷ M. Krawczyk, S. Mamica, M. Mruczkiewicz, J. W. Klos, S. Tacchi, M. Madami, G. Gubbiotti, G. Duerr, and D. Grundler, J. Phys. D: Appl. Phys. **46**, 495003 (2013).
- ⁸ F. Montoncello, S. Tacchi, L. Giovannini, M. Madami, G. Gubbiotti, G. Carlotti, E. Sirotkin, E. Ahmad, F. Y. Ogrin, and V. V. Kruglyak, Appl. Phys. Lett. **102**, 202411 (2013).
- ⁹ M. Kostylev, P. Schrader, R. L. Stamps, G. Gubbiotti, G. Carlotti, A. O. Adeyeye, S. Goolaup, and N. Singh, Appl. Phys. Lett. **92**, 132504 (2008).
- ¹⁰ K.-S. Lee, D.-S. Han, and S.-K. Kim, Phys. Rev. Lett. **102**, 127202 (2009).
- ¹¹ Z. K. Wang, V. L. Zhang, H. S. Lim, S. C. Ng, M. H. Kuok, S. Jain, and A. O. Adeyeye, Appl. Phys. Lett. **94**, 083112 (2009).
- ¹² Z. K. Wang, V. L. Zhang, H. S. Lim, S. C. Ng, M. H. Kuok, S. Jain, and A. O. Adeyeye, ACS Nano **4**, 643 (2010).
- ¹³ F. S. Ma, H. S. Lim, V. L. Zhang, S. C. Ng, and M. H. Kuok, Nanoscale Res. Lett. **7**, 1 (2012).
- ¹⁴ D. Kumar, J. W. Klos, M. Krawczyk, and A. Barman, J. Appl. Phys. **115**, 043917 (2014).
- ¹⁵ A. V. Chumak, V. S. Tiberkevich, A. D. Karenowska, A. A. Serga, J. F. Gregg, A. N. Slavin, and B. Hillebrands, Nat. Commun. **1**, 141 (2010).
- ¹⁶ M. Vogel, A. V. Chumak, E. H. Waller, T. Langner, V. I. Vasyuchka, B. Hillebrands, and G. von Freymann, Nat. Phys. **11**, 487 (2015).
- ¹⁷ J. Topp, D. Heitmann, M. P. Kostylev, and D. Grundler, Phys. Rev. Lett. **104**, 207205 (2010).
- ¹⁸ S. Tacchi, M. Madami, G. Gubbiotti, G. Carlotti, S. Goolaup, A. O. Adeyeye, N. Singh, and M. P. Kostylev, Phys. Rev. B **82**, 184408 (2010).
- ¹⁹ J. Topp, S. Mendach, D. Heitmann, M. Kostylev, and D. Grundler, Phys. Rev. B **84**, 214413 (2011).
- ²⁰ J. Ding, M. Kostylev, and A. O. Adeyeye, Phys. Rev. Lett. **107**, 047205 (2011).
- ²¹ C. S. Lin, H. S. Lim, V. L. Zhang, Z. K. Wang, S. C. Ng, M. H. Kuok, M. G. Cottam, S. Jain, and A. O. Adeyeye, Journal of Applied Physics **111**, 033920 (2012).
- ²² K. Di, S. X. Feng, S. N. Piramanayagam, V. L. Zhang, H. S. Lim, S. C. Ng, and M. H. Kuok, Sci. Rep. **5**, 10153 (2015).
- ²³ H. Yu, G. Duerr, R. Huber, M. Bahr, T. Schwarze, F. Brandl, and D. Grundler, Nat. Commun. **4**, 2702 (2013).
- ²⁴ M. P. Kostylev, A. A. Serga, T. Schneider, B. Leven, and B. Hillebrands, Appl. Phys. Lett. **87**, 153501 (2005).
- ²⁵ K.-S. Lee and S.-K. Kim, J. Phys. D: Appl. Phys. **104**, 053909 (2008).
- ²⁶ A. Khitun, M. Bao, and K. L. Wang, J. Phys. D: Appl. Phys. **43**, 264005 (2010).
- ²⁷ K. Vogt, F. Fradin, J. Pearson, T. Sebastian, S. Bader, B. Hillebrands, A. Hoffmann, and H. Schultheiss, Nat. Commun. **5**, 3727 (2014).
- ²⁸ S.-K. Kim, K.-S. Lee, and D.-S. Han, Appl. Phys. Lett. **95**, 082507 (2009).
- ²⁹ M. Inoue, A. Baryshev, H. Takagi, P. B. Lim, K. Hatafuku, J. Noda, and K. Togo, Appl. Phys. Lett. **98**, 132511 (2011).
- ³⁰ M. Langer, K. Wagner, T. Sebastian, R. Hübner, J. Grenzer, Y. Wang, T. Kubota, T. Schneider, S. Stienen, K. Lenz, H. Schultheiss, J. Lindner, K. Takanashi, R. E. Arias, and J. Fassbender, Appl. Phys. Lett. **108**, 102402 (2016).
- ³¹ I. Barsukov, F. M. Römer, R. Meckenstock, K. Lenz, J. Lindner, S. Hemken to Krax, A. Banholzer, M. Körner, J. Grebing, J. Fassbender, and M. Farle, Phys. Rev. B **84**, 140410 (2011).
- ³² P. Landeros and D. L. Mills, Phys. Rev. B **85**, 054424 (2012).
- ³³ R. A. Gallardo, A. Banholzer, K. Wagner, M. Körner, K. Lenz, M. Farle, J. Lindner, J. Fassbender, and P. Landeros, New J. Phys. **16**, 023015 (2014).
- ³⁴ H. Lichte, Ultramicroscopy **108**, 256 (2008).
- ³⁵ B. A. Kalinikos and A. N. Slavin, J. Phys. C **19**, 7013 (1986).

- ³⁶ M. L. Sokolovskyy and M. Krawczyk, *J. Nanopart. Res.* **13**, 6085 (2011).
- ³⁷ J. W. Kłos, D. Kumar, J. Romero-Vivas, H. Fangohr, M. Franchin, M. Krawczyk, and A. Barman, *Phys. Rev. B* **86**, 184433 (2012).
- ³⁸ R. A. Gallardo, M. Langer, A. Roldán-Molina, T. Schneider, K. Lenz, J. Lindner, and P. Landeros, *ArXiv: 1610.04176* (2016).
- ³⁹ A. Vansteenkiste, J. Leliaert, M. Dvornik, M. Helsen, F. Garcia-Sanchez, and B. Van Waeyenberge, *AIP Adv.* **4**, 107133 (2014).
- ⁴⁰ K. Wagner, S. Stienen, and M. Farle, *ArXiv: 1506.05292* (2015).
- ⁴¹ R. D. McMichael and M. D. Stiles, *J. Appl. Phys.* **97**, 10J901 (2005).
- ⁴² M. Lehmann and H. Lichte, *Microscopy and Microanalysis* **8**, 447 (2002).
- ⁴³ M. Körner, F. Röder, K. Lenz, M. Fritzsche, J. Lindner, H. Lichte, and J. Fassbender, *Small* **10**, 5161 (2014).
- ⁴⁴ K. Harada, A. Tonomura, Y. Togawa, T. Akashi, and T. Matsuda, *Applied Physics Letters* **84**, 3229 (2004).
- ⁴⁵ E. Snoeck, F. Houdellier, Y. Taniguchi, A. Masseboeuf, C. Gatel, J. Nicolai, and M. Hytch, *Microscopy and Microanalysis* **20**, 932 (2014).
- ⁴⁶ M. Körner, K. Lenz, R. A. Gallardo, M. Fritzsche, A. Mücklich, S. Facsko, J. Lindner, P. Landeros, and J. Fassbender, *Phys. Rev. B* **88**, 054405 (2013).
- ⁴⁷ K. Lenz, E. Kosubek, K. Baberschke, H. Wende, J. Herfort, H.-P. Schönherr, and K. H. Ploog, *Phys. Rev. B* **72**, 144411 (2005).
- ⁴⁸ J. Lindner, D. E. Bürgler, and S. Mangin, in *Magnetic Nanostructures* (Springer, 2013) pp. 1–35.
- ⁴⁹ P. Perkes, Arizona State University (ASU), *AZ* **111**, 290 (2002).
- ⁵⁰ F. Röder, A. Lubk, D. Wolf, and T. Niermann, *Ultramicroscopy* **144**, 32 (2014).
- ⁵¹ A. Tonomura, T. Matsuda, J. Endo, T. Arii, and K. Mihami, *Phys. Rev. B* **34**, 3397 (1986).